Thin Solid Films 529 (2013) 407–411

Contents lists available at SciVerse ScienceDirect

Thin Solid Films

journal homepage: www.elsevier.com/locate/tsf

Improved surface corrosion resistance of WE43 magnesium alloy by dual titanium and oxygen ion implantation

Ying Zhao [a,b], Guosong Wu [b], Qiuyuan Lu [b], Jun Wu [a], Ruizhen Xu [b], Kelvin W.K. Yeung [a,*], Paul K. Chu [b,**]

[a] Department of Orthopaedics & Traumatology, The University of Hong Kong, Pokfulam, Hong Kong, China
[b] Department of Physics and Materials Science, City University of Hong Kong, Tat Chee Avenue, Kowloon, Hong Kong, China

ARTICLE INFO

Available online 29 May 2012

Keywords:
Magnesium alloys
Biomaterials
Ion implantation
Corrosion resistance
Surface

ABSTRACT

Magnesium alloys are potential biodegradable materials and have attracted much attention due to their outstanding biological performance and mechanical properties. However, their rapid degradation inside the human body cannot meet clinical needs. In order to improve the corrosion resistance, dual titanium and oxygen ion implantation is performed to modify the surface of the WE43 magnesium alloy. X-ray photoelectron spectroscopy is used to characterize the microstructures in the near surface layer and electrochemical impedance spectroscopy, potentiodynamic polarization, and immersion tests are employed to investigate the corrosion resistance of the implanted alloys in simulated body fluids. The results indicate that dual titanium and oxygen ion implantation produces a TiO_2-containing surface film which significantly enhances the corrosion resistance of WE43 magnesium alloy. Our data suggest a simple and practical means to improve the corrosion resistance of degradable magnesium alloys.

1. Introduction

Metal materials such as titanium alloys and stainless steels are widely used in bone fracture fixation or bone deformity repair due to their good mechanical properties and corrosion resistance [1–3]. However, the need for repeated surgery for implant removal and complicated surgical procedures increases the costs and risks to patients [4,5]. Development of biodegradable materials is a desirable advancement and among the various biodegradable materials, metallic materials such as magnesium alloys are preferable for orthopedic implants because their mechanical properties are closer to those of human bones [6,7]. The current major obstacle hampering wider acceptance is the rapid degradation of magnesium alloys inside the human body and hydrogen evolution during degradation [8–14]. Therefore, the corrosion rate must be controlled before magnesium alloys can be safely used in clinical applications.

Ion implantation has been utilized to control the degradation rate of magnesium and its alloys [15–17]. Considering future in vivo applications, titanium ion implantation is a good means due to the excellent corrosion resistance and biocompatibility of titanium. Liu et al. [18] conducted titanium ion implantation to suppress fast degradation of AZ91 magnesium alloy in a physiological environment and got some inspiring results. In the case of metal ion implantation, improvement in the corrosion resistance is often related to the formation of a corrosion resistant metal oxide and the dramatically reduced magnesium content in the top surface implanted layer [19]. TiO_2 is chemically stable and its existence in the surface layer can enhance the corrosion resistance [20]. However, after titanium ion implantation, it is still necessary to further modify the sample surface to enable optimal formation of TiO_2. As a non-line-of-sight technique, oxygen plasma immersion ion implantation (PIII) is particularly suitable for biomedical implants with a complex geometry [21,22] and is expected to promote oxidation of titanium. In this work, titanium ion implantation and subsequent oxygen PIII are conducted to modify degradable WE43 (Mg-Y-RE) magnesium alloy. Polarization tests, electrochemical impedance spectroscopy (EIS), and immersion tests are used to investigate the corrosion behavior of the surface modified magnesium alloy in simulated body fluids (SBF).

2. Experimental details

The as-cast WE43 magnesium alloy (3.83 wt.% Y, 2.47 wt.% Nd, 1.20 wt.% Zr, 0.12 wt.% Zn, and balance Mg) was cut into blocks with dimensions of $10\times10\times5$ mm. The samples were mechanically polished using up to 5 μm diamond paste, ultrasonically washed in ethanol, and dried before undergoing titanium ion implantation in an HEMII-80 ion implanter equipped with a titanium cathodic arc source in the Plasma Laboratory in City University of Hong Kong. The samples were implanted for 0.5 h at a terminal voltage of 20 kV and base pressure of 1.5×10^{-3} Pa. The ion implant fluence was about 7.3×10^{16} ions.cm^{-2}. Some of the Ti-implanted samples were randomly selected for subsequent oxygen PIII in a GPI-100 ion implanter. Oxygen was introduced at a flow rate of 30 sccm and the plasma was triggered by 1000 W radio frequency (RF). Using a pulsed voltage of 25 kV, pulse width of 30 μs, and pulsing frequency of 120 Hz, oxygen PIII was conducted for 3 h.

* Corresponding author. Tel.: +852 22554654; fax: +852 28174392.
** Corresponding author. Tel.: +852 34427724; fax: +852 34420542.
E-mail addresses: wkkyeung@hku.hk (K.W.K. Yeung), paul.chu@cityu.edu.hk (P.K. Chu).

0040-6090/$ – see front matter © 2012 Elsevier B.V. All rights reserved.
doi:10.1016/j.tsf.2012.05.046

The elemental chemical states and depth profiles before and after ion implantation were determined by X-ray photoelectron spectroscopy (XPS, Physical Electronics PHI 5802) using a monochromatic Al K_α radiation source. High-resolution scans were obtained at a constant pass energy of 58.70 eV, take-off angle of 45°, and step size of 0.25 eV. The depth profiles were obtained by argon ion sputtering at 2 kV acceleration voltage from a rastered area of 2 mm × 2 mm. Under the same condition, the sputtering rate was estimated to be about 4 nm·min^{-1} for a SiO_2 standard sample. The depth scale was estimated based on this sputtering rate in this study. The binding energies were referenced to the C 1s line at 285.0 eV and a Gaussian–Lorentzian peak fitting model was adopted to deconvolute the Ti 2p spectra. The atom concentration of each element was calculated using the following formula [23]:

$$C_x = \frac{I_x/S_x}{\sum I_i/S_i},$$

where C_x is the atomic concentration of element x, I represents the intensity, and S_x denotes the sensitivity factor of element x. In this study, the sensitivity factors of the Mg 1s, Ti 2p, O 1s and Y 3d peaks were 1.035, 2.077, 0.733, and 2.343, respectively.

The electrochemical corrosion characteristics were determined in an acellular SBF with a pH of 7.40 (ion concentrations of Na^+ 142.0, K^+ 5.0, Mg^{2+} 1.5, Ca^{2+} 2.5, Cl^- 147.8, HCO_3^- 4.2, HPO_4^{2-} 1.0, and SO_4^{2-} 0.5 mM similar to those of human blood plasma [24]) at 37 °C using a Zahner Zennium electrochemical workstation based on the conventional three-electrode technique. The potential was referenced to a saturated calomel electrode (SCE) and the counter electrode was a platinum sheet. All the specimens were mounted using silicon rubber (704 RTV Silicon, China) and only a surface area of 10 × 10 mm^2 was exposed to the SBF. The EIS data were recorded from 100 kHz to 100 mHz with a 10 mV sinusoidal perturbing signal at the open-circuit potential after stabilization in the solution for 5 min. After the EIS measurement, the polarization curves were immediately measured by scanning the potential from −150 mV to 600 mV at a rate of 1 mV/s. Since there were limitations in electrochemical techniques to elucidate the details of the corrosion behavior [25], immersion tests were further performed. After the samples were soaked in the SBF at 37 °C for 3 h, the surface morphology was examined by scanning electron microscopy (SEM, JEOL JSM-820 operated at 20 kV).

3. Results and discussion

The XPS depth profiles and high resolution XPS Ti 2p, Mg 1s, O 1s, and Y 3d spectra obtained from the Ti-implanted and Ti–O implanted WE43 are depicted in Figs. 1 and 2, respectively. As shown in Fig. 1a, there is a thin Ti-containing layer about 64 nm thick on the Ti-implanted sample and the depth profile of the implanted titanium shows a Gaussian shape. Prior to analyzing the XPS Ti 2p spectrum, the oxygen valance state of the outermost surface should be firstly examined to determine whether the sample surface is contaminated or not. As shown in Fig. 2a, the high resolution XPS O 1s spectrum of the outermost surface can be deconvoluted into three peaks corresponding to TiO_2 (530.2 eV), MgO (530.8 eV) and adsorbed H_2O (532.8 eV) [26]. After removing the surface contaminated materials (sputtering for 4 min), the high resolution XPS Ti 2p spectrum (Fig. 2a) is acquired and deconvoluted into several components at binding energies 458.9 eV, 456.9 eV, 455.1 eV, and 454.3 eV corresponding to TiO_2, Ti_2O_3, TiO, and Ti, respectively [26]. The dominant surface valence state is Ti^0 and the small quantity of titanium oxide is attributed to the non-UHV (ultra-high vacuum) conditions in our PIII instrument [22,27]. With sputtering, the Ti 2p peak shifts to a lower binding energy, indicating that oxidized titanium (Ti^{4+}, Ti^{3+} and Ti^{2+}) decreases gradually and metallic one (Ti^0) increases gradually up to a depth of 32 nm. Afterwards, the titanium (Ti^0) concentration declines gradually to zero. The high resolution XPS Mg 1s and O 1s spectra show that the valence states of magnesium gradually change from oxidized to metallic ones, accompanied by gradually declined O 1s intensity upon sputtering (Fig. 2a). It thus can be inferred that titanium and magnesium in the near surface are oxidized.

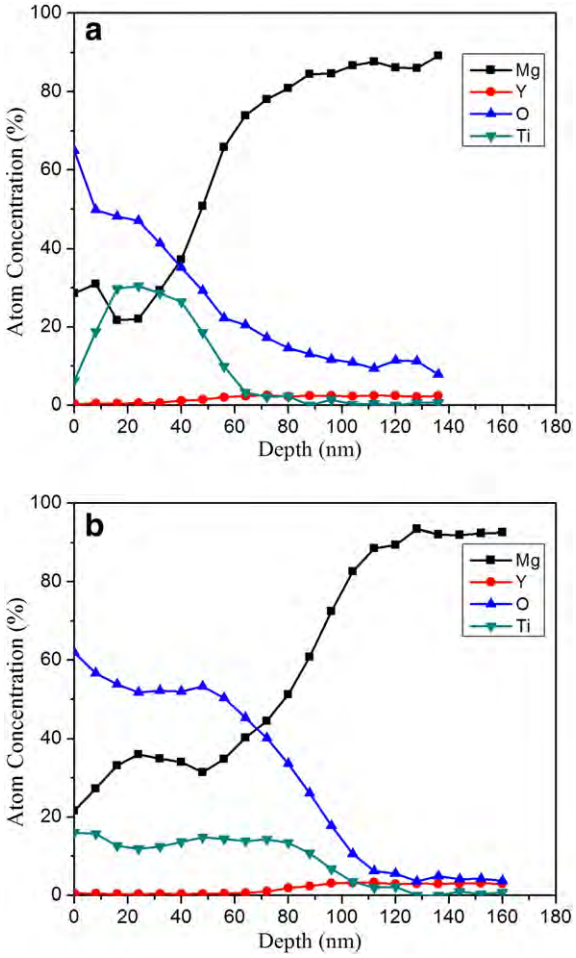

Fig. 1. XPS depth profiles of (a) Ti-implanted WE43 and (b) Ti–O implanted WE43.

In comparison with the Ti-implanted sample, a higher relative content of oxygen is observed from the Ti–O implanted sample. Titanium exhibits a more even distribution with a peak concentration of about 15 at.% and the depth increases from about 64 nm to 104 nm (Fig. 1b). The high resolution XPS Ti 2p spectrum acquired after sputtering for 4 min reveals that TiO_2 is predominant in the implanted layer, although traces of other chemical states such as Ti^{3+} (Ti_2O_3) and Ti^{2+} (TiO) can also be detected. In fact, there should be more TiO_2 in the implanted layer, because TiO_2 might be deoxidized to Ti_2O_3 and TiO under argon ion bombardment [28,29]. Following the analysis of Fig. 2a, the shift in the Ti 2p and Mg 1s peak upon sputtering indicates that the near surface of the implanted sample is oxidized and a thicker oxide layer (~80 nm) composed of mainly TiO_2 and MgO is formed on the Ti–O implanted WE43. It is noted that dual titanium and oxygen ion implantation can reduce the surface magnesium content and a trace of yttrium is observed from the modifier layer. Reduction in the amount of reactive magnesium may enhance the corrosion resistance [19]. The absence of yttrium may be attributed to the decrease in the relative content of yttrium after implantation.

Fig. 3 depicts typical polarization curves of the WE43 alloys before and after implantation. Generally, the cathodic side of the polarization curve is considered to represent the cathodic hydrogen evolution, whereas the anodic one represents the dissolution of magnesium in the solution [30,31]. The corrosion potential and corrosion current density can be derived directly from the corresponding region in the cathodic polarization curves by Tafel region extrapolation. According to the

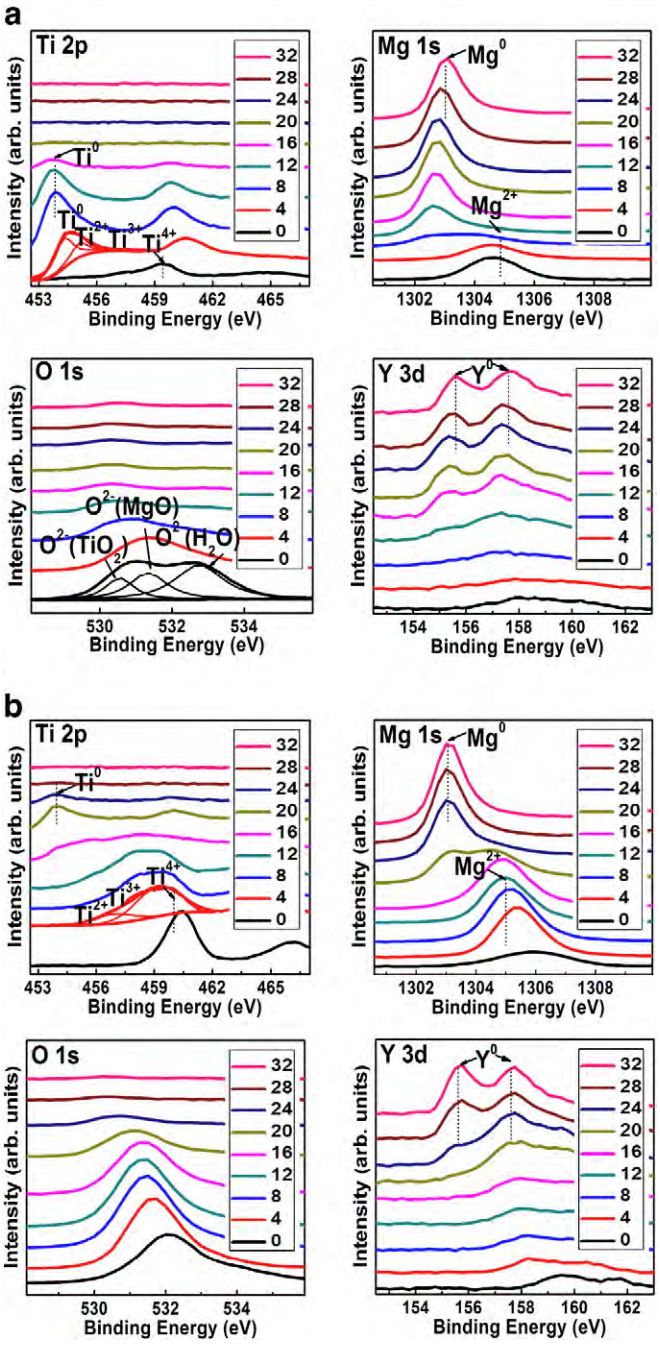

Fig. 2. High-resolution XPS spectra acquired from the (a) Ti-implanted WE43 and (b) Ti–O implanted WE43 at different sputtering time (the numbers in the figures denoting the sputtering time).

deduction from the cathodic side of the curves, the corrosion current densities measured from the Ti–O implanted WE43, Ti-implanted WE43, and un-implanted WE43 are 1.44×10^{-5} A/cm^2, 6.99×10^{-5} A/cm^2, and 3.27×10^{-4} A/cm^2, respectively. The results suggest that the hydrogen evolution rate from the Ti–O implanted and Ti-implanted WE43 is much smaller than that from the un-implanted WE43 sample, especially Ti–O implanted WE43 which shows the smallest rate of electrochemical degradation. The anodic sides of the curve for the three samples are also different. When the potential reaches −1.545 V/SCE (film breakdown potential), the corrosion current density of the Ti–O implanted WE43 increases rapidly. It implies that there is a protective oxide film on the sample surface to retard corrosion [31]. When the anodic potential reaches the film breakdown potential, the surface film is fractured and magnesium corrosion is accelerated [32]. As for the Ti-

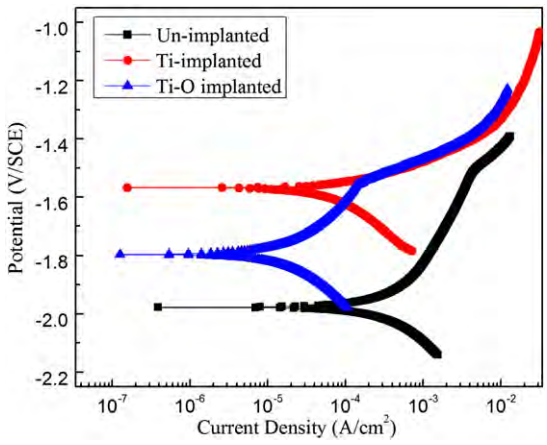

Fig. 3. Polarization curves of un-implanted WE43, Ti-implanted WE43 and Ti–O implanted WE43 in SBF.

implanted and un-implanted WE43, there is no apparent change in the current in the polarization curves, suggesting the lack of protective effects from the surface oxide film.

Fig. 4 presents the immersion test results. After immersion in SBF for 3 h, general corrosion is observed from the surface of the un-implanted WE43 as manifested by a number of homogeneously distributed white corrosion products and networks of cracks shown in Fig. 4a and b. The EDS (energy-dispersive X-ray spectroscopy) results in Fig. 4a reveal that the white corrosion products are rich in O, Mg, P, and Ca and may be due to precipitation of MgO and/or $Mg(OH)_2$, phosphates, and carbonates which are usually present as amorphous phases [33–35]. The formation of cracks may be due to dehydration of the corrosion products [36]. Fig. 4c and d exhibits the typical morphology of the Ti-implanted WE43 with localized corrosion. It is characterized by inhomogeneous white corrosion products at low magnification and round corrosion pits at high magnification. In comparison with the un-implanted WE43, most areas on the Ti-implanted WE43 are smooth without showing severe corrosion attack and there are only small amounts of corrosion products with a larger size. It implies that corrosion in the localized vulnerable area is quite serious after titanium ion implantation. The EDS results in Fig. 4c disclose that the surface corrosion products are composed of O, Mg, P, and Ca and similar to those on the un-implanted WE43. Among the three samples, Ti–O implanted WE43 shows the least degree of corrosion. The sample surface is quite uniform and smooth and only small quantities of corrosion pits and white round particles are visible in the localized regions (Fig. 4e and f). The immersion tests disclose that the Ti–O implanted WE43 degrades most slowly among the three samples and the trend is consistent with that inferred from the electrochemical results. In addition, localized corrosion becomes the dominant mechanism instead of general corrosion after surface modification.

The representative EIS spectra (Nyquist plots) acquired from the un-implanted WE43, Ti-implanted WE43, and Ti–O implanted WE43 after soaking in SBF for 5 min are presented in Fig. 5. Two capacitive arcs, one in the high frequency region and the other in the low frequency region, are visible in the spectrum of the un-implanted WE43. The high frequency behavior is usually related to an electric double layer and the low frequency capacitance arc reflects surface film effects [36]. After ion implantation, the capacitive arcs are evidently enlarged. The diameter of the capacitive arc observed from the Ti-implanted WE43 is almost 4 orders of magnitude larger than that of the un-implanted WE43, whereas that of the Ti–O implanted WE43 is almost 5 orders of magnitude bigger than that of the Ti-implanted WE43. It is known that a larger diameter arc represents better corrosion resistance and hence, the EIS results indicate that dual titanium and oxygen ion implantation can significantly improve the corrosion resistance of WE43.

Taking the physical structure of the electrode system and its impedance response into account, two equivalent circuits (EC) are employed

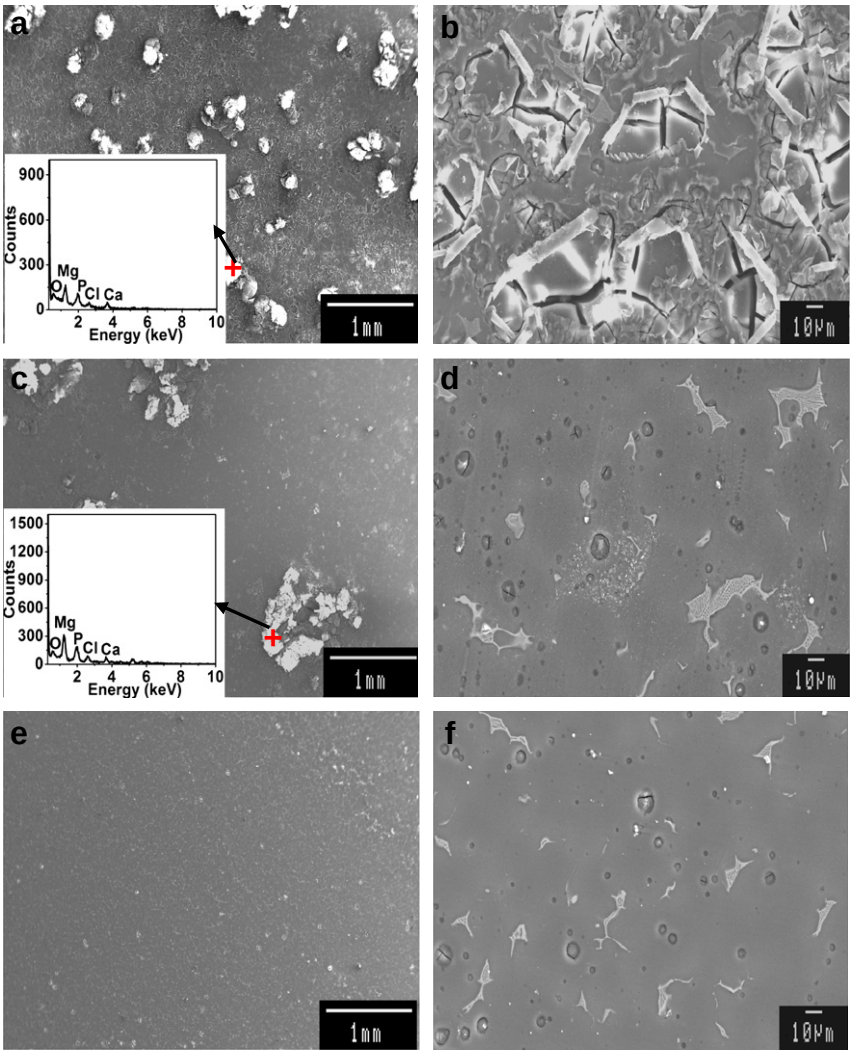

Fig. 4. Surface morphology of WE43 magnesium alloys after immersion in simulated body fluid for 3 h: (a, b) un-implanted WE43; (c, d) Ti-implanted WE43; (e, f) Ti–O implanted alloy. (The graphs in the lower left of panel a and panel c are EDS spectra of the marked white corrosion products. Panels b, d and f are local enlargement of panels a, c and e in the area of the substrate.)

to model the un-implanted WE43 alloy/solution system and implanted WE43 alloy/solution system. The results are displayed in Fig. 5a and b, respectively. C_f, one of the constant phase element (CPE) components,

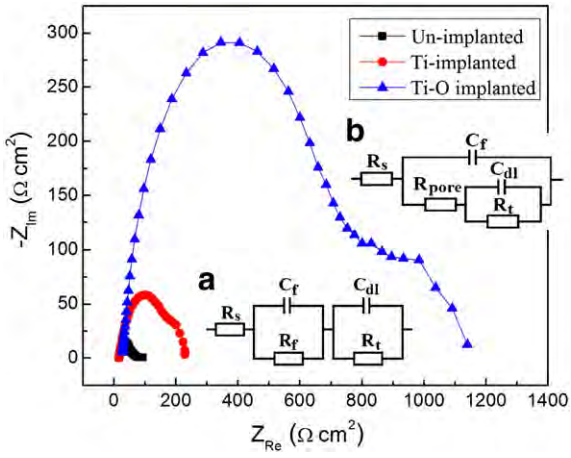

Fig. 5. Representative EIS spectra (Nyquist plots) and corresponding equivalent circuit (EC) of un-implanted WE43, Ti-implanted WE43 and Ti–O implanted WE43 after soaking in SBF for 5 min. (a) EC for the un-implanted WE43; (b) EC for Ti-implanted and Ti–O implanted WE43.

represents the capacitance of the surface film and R_f is the corresponding film resistance. C_{dl}, another component of CPE, expresses the electric double layer capacity in the vulnerable regions and R_t is the charge transfer resistance related to the electrochemical reaction in the same region. C_{dl} (or C_f) is usually defined by two values, Y_0 and n. When n is equal to 1, C_{dl} (or C_f) is identical to a capacitor. R_s represents the solution resistance between the reference and working electrodes and R_{pore} is the sum of the resistances of all the pores in the surface film. The fitted results of the WE43 alloy are listed in Table 1. R_t of the Ti–O implanted sample is the largest, followed by the Ti-implanted sample and the un-implanted sample showing the least. Similarly, R_{pore} of the implanted sample is also significantly enhanced compared to R_f before implantation. The results reveal that ion implantation reduces the corrosion rate of WE43 and in particular, dual titanium and oxygen ion implantation significantly improves the corrosion resistance of WE43 due to the formation of a TiO_2-containing oxide film.

The large degradation rates of magnesium alloys in SBF primarily originate from aggressive attack by chloride ions. As reported in the literature [37], $Mg(OH)_2$ and MgO are usually formed on the surface of magnesium alloys after exposure to air. However, the native oxidized surface layer is loose and cannot provide sufficient protection for the substrate. Chloride ions can easily transform the $Mg(OH)_2$ into more soluble $MgCl_2$ accelerating dissolution of the substrate. Therefore, corrosion spreads quickly on the entire surface. Titanium incorporation is

Table 1
Fitted EIS results of WE43 magnesium alloy in SBF.

	R_s (Ω cm^2)	Y_{0f} (Ω^{-1} cm^{-2} s^{-n})	n_f	R_f or R_{pore} (Ω cm^2)	Y_{0d1} (Ω^{-1} cm^{-2} s^{-n})	n_{dl}	R_t (Ω cm^2)
Un-implanted	16.29	2.022E−3	0.9011	10.68	5.073E−5	0.7986	40.28
Ti-implanted	16.82	1.709E−2	1	33.36	7.501E−5	0.76	173.1
Ti–O implanted	26.24	1.783E−4	0.8877	266.8	2.179E−6	0.8656	743.1

expected to passivate the surface of WE43, but since ion implantation unavoidably produces some vulnerable regions on the surface, localized galvanic corrosion occurs and propagates underneath rapidly. It is postulated that the titanium rich regions serve as the cathode with the magnesium matrix being the anode in the galvanic cell when aggressive SBF penetrates the surface. Subsequent oxygen PIII produces a much thicker oxide layer composed of titanium oxide and magnesium oxide on the surface. The homogeneous TiO_2 passivates the WE43 surface and provides a good barrier that resists attack by the aggressive media. Our results reveal that surface degradation of WE43 can be controlled by the modified oxide layer.

4. Conclusion

Dual titanium and oxygen ion implantation is conducted to alter the surface degradation behavior of WE43 magnesium alloys. Introduction of titanium stabilizes the WE43 to some extent, but localized severe galvanic effects produce vulnerable regions. Formation of a TiO_2-containing surface film by subsequent oxygen ion implantation provides a better barrier to resist the attack of aggressive SBF. Our results indicate that dual titanium and oxygen ion implantation is a promising surface modification technique for WE43 magnesium alloy.

Acknowledgments

This work was jointly supported by HKU Seed Funding for Basic Research as well as Hong Kong Research Grants Council (RGC) General Research Funds (GRF) #718507, #123708, and #112510.

References

[1] X.Y. Liu, P.K. Chu, C.X. Ding, Mater. Sci. Eng., R 47 (2004) 49.
[2] G. Voggenreiter, S. Leiting, H. Brauer, P. Leiting, M. Majetschak, M. Bardenheuer, U. Obertacke, Biomaterials 24 (2003) 247.
[3] Y. Zhao, T.Y. Xiong, W.H. Huang, Appl. Surf. Sci. 256 (2010) 3073.
[4] C. Castellani, R.A. Lindtner, P. Hausbrandt, E. Tschegg, S.E. Stanzl-Tschegg, G. Zanoni, S. Beck, A.M. Weinberg, Acta Biomater. 7 (2011) 432.
[5] A. Weiler, R.F.G. Hoffmann, A.C. Stähelin, H.J. Helling, N.P. Südkamp, Arthroscopy 16 (2000) 305.
[6] M.P. Staiger, A.M. Pietak, J. Huadmai, G. Dias, Biomaterials 27 (2006) 1728.
[7] E.L. Zhang, L. Yang, J.W. Xu, H.Y. Chen, Acta Biomater. 6 (2010) 1756.
[8] B. Zberg, P.J. Uggowitzer, J.F. Löffler, Nat. Mater. 8 (2009) 887.
[9] F. Witte, J. Fischer, J. Nellesen, C. Vogt, J. Vogt, T. Donath, F. Beckmann, Acta Biomater. 6 (2010) 1792.
[10] G. Song, Adv. Eng. Mater. 7 (2005) 563.
[11] X. Gu, Y. Zheng, S. Zhong, T. Xi, J. Wang, W. Wang, Biomaterials 31 (2010) 1093.
[12] G. Song, A. Atrens, Adv. Eng. Mater. 1 (1999) 11.
[13] G. Song, A. Atrens, M. Dargusch, Corros. Sci. 41 (1999) 249.
[14] A. Atrens, M. Liu, N.I. Zainal Abidin, Mater. Sci. Eng., B 176 (2011) 1609.
[15] C.L. Liu, Y.C. Xin, X.B. Tian, P.K. Chu, Thin Solid Films 516 (2007) 422.
[16] M.K. Lei, P. Li, H.G. Yang, X.M. Zhu, Surf. Coat. Technol. 201 (2007) 5182.
[17] Y. Zhao, G.S. Wu, H.B. Pan, K.W.K. Yeung, P.K. Chu, Mater. Chem. Phys. 132 (2012) 187.
[18] C.L. Liu, Y.C. Xin, X.B. Tian, J. Zhao, P.K. Chu, J. Vac. Sci. Technol., A 25 (2007) 334.
[19] Y.C. Xin, P.K. Chu, in: H.S. Dong (Ed.), Surface Engineering of Light Alloys—Aluminium, Magnesium and Titanium Alloys, CRC Press and Woodhead Publishing, Abington, UK, 2010, p. 393, (Chapter 11).
[20] J. Pan, C. Leygraf, D. Thierry, A.M. Ektessabi, J. Biomed. Mater. Res. 35 (1997) 309.
[21] P.K. Chu, Surf. Coat. Technol. 201 (2007) 5601.
[22] P.K. Chu, J. Vac. Sci. Technol. B 22 (2004) 289.
[23] J.F. Moulder, W.F. Stickle, P.E. Sobol, K.D. Bomben, J. Chastain, Perkin-Elmer Corporation, Minnesota, USA, 1992, p. 25.
[24] T. Kokubo, H. Kushitani, S. Sakka, T. Kitsugi, T. Yamamuro, J. Biomed. Mater. Res. 24 (1990) 721.
[25] Z. Shi, M. Liu, A. Atrens, Corros. Sci. 52 (2010) 579.
[26] http://srdata.nist.gov/.
[27] R.W.Y. Poon, K.W.K. Yeung, X.Y. Liu, P.K. Chu, C.Y. Chung, W.W. Lu, K.M.C. Cheung, D. Chan, Biomaterials 26 (2005) 2265.
[28] S. Hashimoto, J. Surf. Anal. 10 (2003) 136.
[29] Y. Sakai, S. Ninomiya, K. Hiraoka, Surf. Interface Anal. 43 (2011) 1605.
[30] Y.S. Wang, C.S. Lim, C.V. Lim, M.S. Yong, E.K. Teo, L.N. Moh, Mater. Sci. Eng., C 31 (2011) 579.
[31] J.W. Chang, X.W. Guo, P.H. Fu, L.M. Peng, W.J. Ding, Electrochim. Acta 52 (2007) 3160.
[32] Y. Song, D. Shan, R. Chen, E. Han, Corros. Sci. 51 (2009) 1087.
[33] S.X. Zhang, X.N. Zhang, C.L. Zhao, J.A. Li, Y. Song, C.Y. Xie, H.R. Tao, Y. Zhang, Y.H. He, Y. Jiang, Y.J. Bian, Acta Biomater. 6 (2010) 626.
[34] Y.C. Xin, K.F. Huo, T. Hu, G.Y. Tang, P.K. Chu, J. Mater. Res. 24 (2009) 2711.
[35] Y.C. Xin, T. Hu, P.K. Chu, J. Electrochem. Soc. 157 (2010) C238.
[36] Y. Song, D. Shan, R. Chen, F. Zhang, E. Han, Mater. Sci. Eng., C 29 (2009) 1039.
[37] M. Liu, S. Zanna, H. Ardelean, I. Frateur, P. Schmutz, G. Song, A. Atrens, P. Marcus, Corros. Sci. 51 (2009) 1115.